Measurement of the quadriceps muscle displacement and strain fields with ultrasound and Digital Image Correlation (DIC) techniques

J.-S. Affagard, P. Feissel, S F Bensamoun

Measurement of the quadriceps muscles displacement and strain fields with ultrasound and Digital Image Correlation (DIC) techniques

J.-S. Affagard[a,b], P. Feissel[b], S.F. Bensamoun[a*]

[a]Université de Technologie de Compiègne, UMR CNRS 7338, BioMécanique et BioIngénierie, Compiègne, France
[b]Université de Technologie de Compiègne, UMR CNRS 7337, Laboratoire Roberval, Compiègne, France
*Corresponding author, e-mail address: sabine.bensamoun@utc.fr.

ABSTRACT

Objectives - In vivo characterization of muscle tissues is necessary to increase the understanding of musculoskeletal pathologies. Currently, few imaging techniques are able to characterize the in vivo mechanical properties of muscle. Thus, the purpose was to couple experimental and numerical tools to characterize the displacement and strain fields. This approach was validated on a phantom and then applied in vivo on thigh muscles.

Materials and methods - An experimental compression device was developed in order to measure the displacement field from a phantom with inclusions, and from quadriceps muscles, using compressed and uncompressed ultrasound acquisitions (9MHz). A diffuse approximation method was used to determine the optimal ZOI (Zone Of Interest) size (4, 8, 16 pixels) allowing for the realization of the DIC with a low noise and a high spatial resolution (about 100µm). Then, the strain field was represented with a diffuse approximation radius, optimized from the theoretical noise.

Results - The in vitro and in vivo displacement fields confirmed the qualitative ultrasound observations. The ZOI size was found optimal at 8 pixels. Then, the diffuse approximation radii were determined at 9 and 13 data points for the phantom and the quadriceps, respectively, providing the strain field cartographies. These cartographies validated the experimental protocol and the displacement field measurement.

Conclusion – The present study revealed the feasibility of the Digital Image Correlation technique to assess the in vivo muscle mechanical behavior, and could be extended to different soft tissues.

Key words — muscle, digital image correlation, ultrasound, displacement and strain fields, diffuse approximation

1. INTRODUCTION

The in vivo identification of the muscle mechanical behavior remained a challenge to better understand the pathologies. Medical imaging techniques such as ultrasound (US) or magnetic resonance imaging (MRI) allow for the characterization of the morphological properties in order to diagnose and follow-up treatments. To complete the structural analysis, dynamic elastography techniques using measurement of shear wave speed in function of frequencies enable the assessment of the muscle viscoelastic properties [1-3]. Moreover, it is well known that muscle tissue is a complex material with nonlinear and quasi incompressible behaviors. Thus, to further analyze these characteristics, experimental tests and numerical tools were used to measure the muscle displacement field.

Quasi-static tests such as traction [4], suction [5, 6] or indentation [7-9] have been performed in order to measure *in vivo* the external displacements of the skin tissue. Subsequently, Finite Element Model Updating (FEMU) was developed to determine the skin elastic behavior. In addition, ultrasound technique was used to better characterize the geometry of the skin and the environmental tissues with suction [10-13] or indentation tests [14-17]. This modeling provided a more accurate identification of the soft tissues. Other studies coupled in vivo mechanical tests with MRI acquisitions to identify the hyperelastic behavior of the arm and calf muscles [18, 19]. This identification was performed from the displacement of the contours of the muscle, bone and adipose tissues.

To further analyze their characteristics, it was proposed that experimental tests and numerical tools could be used to measure the muscle displacement field and strain fields. Thus, Zerhouni et al. [20] used the MR tagging to measure the 2D myocardial motion during the cardiac cycle. Recently, this method was coupled with quasi-static excitations performed on the lower leg [21] in order to obtain the displacement and strain fields. In addition, a 3D analysis was also carried out on the arm [22, 23]. Moreover, an ultrasound technique was associated with static compression tests on phantom to image the cartography of the strain field in order to calculate the Young's modulus as the stress / strain ratio [24-27]. Ultrasound was further

improved with an algorithm based on the correlation of B-mode ultrasound signals to measure the displacement and strain fields [28, 29]. This measurement was performed on phantom [30-32] and on breast tissue to image the hyperelastic properties and to discern tumors [30, 33, 34]. Another way to measure the displacement field was to use the digital image correlation (DIC) [35-37] that enables to measure the displacement field from images. Thus, Han et al. [38] acquired ultrasound images on phantom, under several static loading, coupled with DIC method to measure the 2D and 3D displacement and strain fields. Moreover, ex-vivo tendon analysis was also performed with DIC to validate 2D ultrasound elastography results, and to demonstrate the potential of the DIC method for the characterization of in vivo biological tissue [37].

Thus, the originality of this study was to use the DIC on ultrasound acquisitions of *in vivo* thigh muscles to obtain a local displacement measurement. Moreover, a home-made compression device was developed to perform a quasi-static loading. Thus, the purpose of this present study was to couple experimental and numerical tools to characterize the displacement and strain fields. This approach was firstly validated on a phantom and then applied in vivo on thigh muscles.

2. MATERIALS AND METHODS

2.1. Experimental set up

A home-made compression device (Fig. 1a-1d) was composed of three plastic plates (200 x 300 mm2). The lower one was only used as a support for the leg and four threaded rods were fixed at each corner allowing the up and down motions of the upper plates. The two upper plates were used to compress the muscle where the level was adjusted with screws. Then, sensors (I-scan, Tekscan, 5027) (Fig. 1d) were placed between the two upper plates in order to quantify the distribution of pressure. A specific design was made on the upper plates to fit and to maintain the ultrasound probe (9MHz) during the loading and the ultrasound acquisitions.

2.2. In vitro and in vivo ultrasound acquisitions

The experimental device was applied in vitro to a phantom (CIRS, Norfolk, VA), mimicking soft tissues, composed of eight spherical inclusions (from #1 to #8) (Diameter: 10 mm and 20 mm) having different stiffnesses (Fig. 1b). The four small and large spheres were aligned and spaced (30 mm) at a depth of 15 mm and 35 mm, respectively. According to the CIRS company, the phantom background had an elasticity of 25 ± 6 kPa and the spherical inclusions had an elasticity of 8 ± 3 kPa (#1, #5), 14 ± 4 kPa (#2, #6), 45 ± 8 kPa (#3, #7), 80 ± 12 kPa (#4, #8) (Fig. 1b).

Subsequently, ultrasound images were acquired for the two central small spherical inclusions (#2, #3) (Fig. 1c).

The homemade compression device was used for *in vivo* experiment performed on the thigh muscles of a 33 year old male without venous pathologies (Fig.1d). The ultrasound probe was placed in the lower third part of the thigh due to the low amount of adipose tissue allowing a better strain of the muscle tissue. Fig. 1e showed the localization of the investigated quadriceps muscles composed of the vastus medialis (VM) and vastus intermedius (VI) (Fig. 1f) acquired with the same optimized ultrasound parameters.

2.3. Measurement of the displacement field with the DIC

The DIC method (Correli_Q4 [36]) is based on the grey level comparison between two B-mode ultrasound (US) acquisitions performed on uncompressed (Fig. 2a, 3a) and compressed (Fig. 2b, 3b) phantom and quadriceps muscle in order to measure the displacement field. The ultrasound parameters were optimized to perform efficiently the digital image correlation (DIC), as described in a previous study [39, 40] where the ultrasound parameters were set up to reduce the random error of the measurement.

A zone of interest (ZOI) was located inside a ROI (region of interest) defined on the ultrasound image (Fig. 1c). The DIC aimed at matching the ZOI (8 pixels) between reference and deformed images. It must be noted that the DIC performances were strongly linked to the grey level and image characteristics (i.e contrast and dynamic of the speckle). Considering *f(x)* and *g(x)*, the grey level values of the reference and deformed images at position *x*, *g(x)* can be defined as:

$$g(x) = f(x + u(x)) + b(x) \tag{1}$$

u(x) is the displacement field and *b(x)* the noise induced by the image acquisition. The specificity of the present global DIC method is to seek the displacement field corresponding to a set of shape function. The field, *u(x)*, can therefore be written as:

$$u(x) = \sum_{a,m} \nu_{am} N_m(x) e_\alpha \tag{2}$$

m is the number of nodes for one element (*m* = 4), $\nu_{\alpha m}$ are the degrees of freedom unknowns of the problem, $N_m(x)$ are the shape functions and e_α is a characteristic vector of the considered element.

To obtain the cartographies representing the lateral (U_x) (Fig. 2c, 3c) and axial (U_y) (Fig. 2d, 3d) displacement fields five ultrasound acquisitions were performed with intermediate loadings (muscle step: 15N, phantom step: 112N). Thus, the DIC convergence was facilitated between the initial (0N) and final (muscle: 60N, phantom: 450N) loadings. These loading level differences were chosen because the same external displacement levels were observed at the sample surface between the two experiments. Finally, the displacement fields were displaced to match the bone structure between the initial and final images. Thus

the femur is taken as the reference.

2.4. Measurement of the strain field

The strain field was calculated using diffuse approximation from the displacement field measurement. This method based on using local least squares [41] consists on performing a local diffuse approximation regression [42, 43]. Thus, cartographies of strain fields were represented for three different ZOI (4, 8 and 16 pixels) with three different diffuse approximation radii (4, 8 and 16 data points) (Fig. 4). These cartographies were obtained for shear strain.

The radius of the diffuse approximation is optimal when the maximum of noise is filtered without losing mechanical information (Fig.5a-5c, 6a-6c). Thus, to determine the more appropriate diffuse approximation radius the standard deviation for each experimental strain (lateral, axial and shear strains) was represented as a function of the radius (from 4 to 20 data points).

Then, the evolution of the theoretical noise filtering, assuming a white Gaussian noise with a standard deviation (σ), can be written in function of a linear operator of the reconstruction (M) [42]:

$$\mathrm{cov}\left(\{\delta u_b\}\right) = \sigma_b^2 M M^T \tag{3}$$

This theoretical curve was shifted in order to match the same value of standard deviation with the experimental curve. Thus, a reference value (dot line) was established to represent the level of the applied filtering. Then, the standard deviation (σ) of the measured displacement field was quantified between 11 uncompressed images by considering a white Gaussian noise for each ZOI (4, 8, 16 pixels).

Finally, the intersection with the theoretical noise filtering revealed the optimal radius for which the cartographies of the lateral, axial and shear strain were represented (Fig. 5d-5f, 6d-6f).

3. RESULTS

3.1. Result of the in vitro and in vivo displacement fields

The ultrasound images acquired on the phantom (Fig. 2a-2b) revealed a higher deformation for the left inclusion (#3) compared to the right (#2) one. This structural result was expected due to the difference of stiffness between the two spherical inclusions.

Fig. 2c and Fig. 2d showed the cartographies of the displacement fields, represented on the uncompressed image, measured along the Y and X axis, respectively.

Along the direction of compression (Fig 2c), highest displacements (about 7mm) were observed (red color) close to surface of the phantom, and lowest displacements (blue color, about 3mm) were found in depth. In addition, a higher gradient of displacement was observed for the left inclusion (#3). This last result was in agreement with the structural deformation observed on the ultrasound acquisitions. Along the X axis (Fig. 2d), the scale indicated few displacements (from -1mm to 0.2mm) which is expected according to the applied compression test. However, a higher gradient displacement field (from -1mm to -0.4mm) was observed in the left inclusion (#3) compared to the right one (#2) (from -0.3mm to -0.1mm).

This last result confirmed the difference of mechanical properties between the two inclusions.

The result of the ultrasound images acquired for the quadriceps muscle (Fig. 3a-3b) revealed a visual sliding of both vasti muscles (VM and VI) around the aponeurosis tissue. The result of the displacement field (Fig. 3c) measured along the Y axis, showed highest displacements (about 10mm, red color) close to the fat tissue while any displacements was found around the bone tissue. Furthermore, a gradient of displacement was observed inside the muscles. Fig. 3d illustrated the cartography of the displacement field measured along the X axis. A high displacement gradient (from -5mm to 2mm), indicated by arrows, was observed around the aponeurosis located between the vastus intermedius (VI) and the vastus medialis (VM) muscles. This last result confirmed the qualitative sliding obtained after the compressive test.

Repeatability (lateral: 1.23 mm, axial: 0.96 mm) and reproducibility (lateral: 0.25 mm, axial: 0.23)

analysis showed similar quantitative and qualitative displacement fields [40].

3.2. Quantification of the experimental noise

Table 1 showed the results of the standard deviation (σ) as a function of the ZOI size (4, 8 and 16 pixels) for the phantom and the quadriceps muscle. As expected, the value of the standard deviation decreases when the ZOI size increase. Along the ultrasound beam (axial direction), the result of the standard deviation was less important than the lateral noise. The comparison between the in vivo and in vitro experimental noises revealed a higher noise for the muscle tissue compared to the phantom.

Table 1: Standard deviation as a function of the ZOI size for the phantom and the quadriceps muscle

	Phantom			Muscle		
ZOI size (pixels)	4	8	16	4	8	16
Axial standard deviation (pixels)	0.83	0.393	0.20	1.46	1.29	0.89
Lateral standard deviation (pixels)	0.99	0.48	0.26	1.98	1.78	1.27

3.3. Result of the in vitro and in vivo strain fields

3.3.1. Determination of the ZOI from the shear strain field

Fig. 4 illustrated the results of the shear strain fields obtained for three different ZOI and three radius of diffuse approximation.

For a ZOI of 4 pixels, the strain field was very noisy and no information can be interpreted (Fig. 4a) with a radius of 4 data points. On the contrary, the spherical inclusions were clearly represented with a radius of 16 data points (Fig. 5c). Nevertheless, the contours of the spherical insertions were not well defined due to the noise.

For a ZOI of 8 pixels, the best cartographies were obtained with a radius between 8 and 16 data points (Fig. 4e-4f). Indeed, these configurations enabled the localization of the two spherical inclusions

represented with clear contours and a quasi-homogeneous strain field [44, 45].

Using a ZOI of 16 pixels, provided a low spatial resolution, the best compromise was represented with a radius of 4 data points (Fig. 4g). For larger radius, the strain field was strongly filtered leading to a lack of information (Fig. 4h-4i).

In agreement with all of these results, a ZOI of 8 pixels was chosen in order to determine the diffuse approximation radius allowing the interpretation of the strain fields.

3.3.2. Analysis of the in vitro strain field with the optimal diffuse approximation radius

The evolution of the experimental standard deviation (σ) was represented for the lateral (Fig. 5b), axial (Fig. 5a) as a function of the radius (blue curve). As expected, the standard deviation decreased exponentially with the radius. The theoretical curve (red) showed the evolution of the standard deviation of the noise.

Fig. 5a revealed that the dotted line intersected the experimental curve (blue) for a radius value of 9 data points. As a consequence, the noise is considered filtered above a radius of 9 data points while below this value the information was degraded. Therefore, the optimal radius was chosen to 9 data points for a ZOI of 8 pixels.

The lateral standard deviation (Fig. 5b) showed that whatever the range of radius is, the experimental curve was always above the dotted line. This last result indicated that the information and the noise were in the same range. Therefore, the lateral strain was not solicited by the present mechanical test.

Thus, the diffuse approximation radius was set up to 9 data points to analyze the strain fields.

The cartographies of the strain fields were represented in the axial (Fig. 5c), lateral (Fig. 5d) and shear (Fig. 5e) directions.

Fig. 5c revealed a high strain field below the left inclusion (#3) while a weak strain field was found below the right inclusion (#2). This result was related to the environmental structure around the inclusions.

Indeed, the strain below the right inclusion (#2) was lower than the strain inside the inclusion, demonstrating that the inclusion was stiffer than the background. On the contrary, the strain below the left inclusion (#3) was higher than the strain inside the inclusion, revealing a softer inclusion than the background.

Fig. 5d was not interpretable due to the low level of information which did not allow the localization of the spherical inclusions.

Fig. 5e showed the shear strain field where the contours of the two inclusions were well identified. In addition, a homogeneous strain was observed inside both inclusions. Therefore, these results confirmed the ultrasound observations and demonstrated the feasibility of the present method to measure the displacement and strain field within the muscle tissue.

3.3.3. Analysis of the in vitro strain field with the optimal diffuse approximation radius

A ZOI of 8 pixels was chosen to analyze the muscle strain fields as previously presented for the phantom.

A similar process as for the in vitro study was performed for the choice of the diffuse approximation radius. A radius of 13 data points was determined as optimal for the in vivo analysis (Fig 6a) and Fig. 6b showed that the information and the noise were in the same range leading more difficult the analysis of the lateral strain field.

Fig. 6c-6e presented the axial, lateral and shear strains of the quadriceps muscle. The three cartographies revealed a sliding of both vastis around the aponeurosis area as it was observed on the ultrasound acquisitions and displacement field (Fig. 3). Moreover, Fig. 7c presented a high strain level located inside the fat tissue, demonstrating a lower stiffness for fat tissue than muscle tissue.

4. DISCUSSION

The originality of this study was to develop an experimental protocol to measure the muscle displacement and the strain field using a DIC. The present protocol was set up on a phantom with structural and mechanical properties know from the CIRS' company. The ultrasound structural deformation observed on the inclusions validated the developed mechanical test and also the displacement field measurement. Furthermore, this in vitro work enabled to fix the ZOI size to 8 pixels due to the clear contours of the inclusions from the strain field. This result allowed to choose a reference ZOI size (8 pixels) for the in vivo study. Moreover, a complementary study was performed on several ZOI sizes and confirmed the use of 8 pixels for the quadriceps muscle.

The comparison of the displacement fields between the phantom (Fig. 2c) and the muscle (Fig. 3c) showed similar maximal axial displacement levels (phantom: -7mmn, muscle: -10mm) despite different loadings were applied. Indeed, a higher loading was performed on the surface of the phantom due to the boundary conditions. In fact, the lateral direction (x axis), the boundary displacement being fixed for the phantom increasing the resulting force. This result demonstrated that the CIRS phantom could be used to mimic the muscle displacement. Obviously, the loadings were adjusted according to the respective mechanical properties. Furthermore, the cartography of axial muscle displacement field (Fig.3c) showed a continuity of the displacement as a function of the muscle depth, and validated the developed experimental protocol (quasi static test and DIC).

On the contrary, the comparison of the lateral displacement (Fig. 2d and Fig. 3d) showed a higher range of displacement values for the muscle (from -5mm to 5mm) compared to the phantom (from -1mm to 1mm). This may be due to the difference of texture. Indeed, a speckle was present on the phantom while the presence of lateral white bands, reflecting the muscle structure, may induce measurement errors on the lateral axis. Moreover, during the mechanical test, a rotation of the muscle structures around the bone and a sliding of the tissue close to the aponeurosis may explain this difference of range.

The quantification of the experimental noise showed a higher incertitude for the lateral displacements

compared to the axial ones for both samples. This result may be due to the direction of the beam which is in the compression direction inducing a higher noise in the lateral direction. The uncertainty of the lateral displacement field lead [34] to propose the identification of the linear and non-linear elasticity of soft tissues from a cost function only based on the axial component.

The comparison of the experimental noise between the phantom and the muscle for both directions revealed a higher error for the muscle tissue due to the difference of texture and due to muscle movements, such as involuntary contraction or blood flow, providing changes during the ultrasound acquisitions.

The method used to determine the diffuse approximation radius was similar to Feissel et al. [46] in order to obtain an optimal filtering. In the present study, the assumption of the white Gaussian noise may induce an error on the diffuse approximation radius choice. Indeed, the DIC method (Correli_Q4), revealing the displacement field as a shape function, provided another reparation of noise [46].

To our knowledge, the DIC is a technique often used in the mechanical field, this study is the first to combine the DIC method with ultrasound acquisition on *in vivo* muscle tissue in order to obtain the strain field. The limitation of the present study is the measurements obtained from one subject and should be realized on other participants. Indeed, the quality of images and the mechanical properties of the muscles will differ between individuals, due to the gender, age and health of muscle. Thus, the measured displacement field might be a starting point for the characterization of the in vivo elastic properties and may be extended to the measurement of different soft tissues. In addition, according the important level of sliding and strain between both vasti muscles, a way to improve the strain cartographies would be to develop an integrated-DIC method to remove the discontinuity problems.

Finally, from this measurement, the next step will be to develop an inverse method, coupling this acquired displacement field with finite element simulation, to identify the muscle mechanical behavior.

ACKNOWLEDGEMENT

This project is co-financed by the European Union engaged in Picardy with the European Regional Development Fund and CNRS (grant Collegium UTC CNRS INSIS).

CONFLICT OF INTEREST STATEMENT

All authors do not have conflict of interest.

REFERENCES

[1] L. Debernard, G. E. Leclerc, L. Robert, F. Charleux, and S. F. Bensamoun, “In vivo characterization of the muscle viscoelasticity in passive and active conditions using multifrequency MR Elastography,” *Journal of Musculoskeletal Research*, vol. 16, no. 2, pp. 1350008-18, 2013

[2] J.-L. Gennisson, T. Deffieux, E. Macé, G. Montaldo, M. Fink, and M. Tanter, “Viscoelastic and anisotropic mechanical properties of in vivo muscle tissue assessed by supersonic shear imaging,” *Ultrasound in medicine & biology*, vol. 36, no. 5, pp. 789-801, 2010.

[3] G. E. Leclerc, F. Charleux, L. Robert, M.-C. Ho Ba Tho, C. Rhein, J.-P. Latrive, and S. F. Bensamoun, “Analysis of liver viscosity behavior as a function of multifrequency magnetic resonance elastography (MMRE) postprocessing,” *Journal of Magnetic Resonance* Imaging, Vol. 38, no. 2, pp. 422–428, 2013.

[4] Y. Mofid, G. Josse, S. Gahagnon, A. Delalleau and F. Ossant, "Mechanical skin thinning-to-thickening transition observed in vivo through 2D high frequency elastography,” *Journal of Biomechanics*, vol. 43, no. 15, pp. 2954-62, 2010.

[5] A. Delalleau, G. Josse, J.-M. Lagarde, H. Zahouani, and J.-M. Bergheau, “A nonlinear elastic behavior to identify the mechanical parameters of human skin in vivo,” *Skin Research and Technology*, vol. 14, no. 2, pp. 152-164, 2008.

[6] M. Kauer, V. Vuskovic, J. Dual, G. Szekely, and M. Bajka, “Inverse finite element characterization of soft tissues,” *Medical Image Analysis*, vol. 6, no. 3, pp. 275-287, 2002.

[7] T. Alja'afreh, “Developing a bio-mechanotronic probing system for estimating soft tissue Young's modulus in vivo,” *Instruments and Experimental Techniques*, vol. 54, no. 1, pp. 131-135, 2011.

[8] A. Delalleau, G. Josse, J.-M. Lagarde, H. Zahouani, and J.-M. Bergheau, “Characterization of the mechanical properties of skin by inverse analysis combined with the indentation test,” *Journal of biomechanics*, vol. 39, no. 9, pp. 1603-1610, 2006.

[9] K. M. Moerman, C. A. Holt, S. L. Evans, and C. K. Simms, “Digital image correlation and finite element modelling as a method to determine mechanical properties of human soft tissue in vivo,” *Journal of biomechanics*, vol. 42, no. 8, pp. 1150-1153, 2009.

[10] S. Diridollou, F. Patat, F. Gens, L. Vaillant, D. Black, J. M. Lagarde, Y. Gall, and M. Berson, “In vivo model of the mechanical properties of the human skin under suction,” *Skin Research and technology*, vol. 6, no. 4, pp. 214-221, 2000.

[11] F. M. Hendriks, D. Brokken, J. T. W. M. Van Eemeren, C. W. J. Oomens, F. P. T. Baaijens, and J. B. A. M. Horsten, “A numerical-experimental method to characterize the non-linear mechanical behaviour of human skin,” *Skin research and technology*, vol. 9, no. 3, pp. 274-283, 2003.

[12] F. M. Hendriks, D. Brokken, C. W. J. Oomens, D. L. Bader, and F. P. T. Baaijens, “The relative contributions of different skin layers to the mechanical behavior of human skin in vivo using suction experiments,” *Medical Engineering and Physics*, vol. 28 no. 3, pp. 259-266, 2006.

[13] J. T. Iivarinen, R. K. Korhonen, P. Julkunen, and J. S. Jurvelin, “Experimental and computational analysis of soft tissue mechanical response under negative pressure in forearm,” *Skin Research and Technology*, pp. 356-365, 2012.

[14] J. T. Iivarinen, R. K. Korhonen, P. Julkunen, and J. S. Jurvelin, “Experimental and computational analysis of soft tissue stiffness in forearm using a manual indentation device,” *Medical engineering & physics*, vol. 33, no. 10, pp. 1245-1253, 2011.

[15] T. K. Koo, J. H. Cohen, and Y. Zheng, “A mechano-acoustic indentor system for in vivo measurement of nonlinear elastic properties of soft Tissue,” *Journal of Manipulative and Physiological Therapeutics*, vol. 34, no. 9, pp. 584-593, 2011.

[16] E. Tönük, and M. B. Silver-Thorn, “Nonlinear elastic material property estimation of lower extremity residual limb tissues, Neural Systems and Rehabilitation Engineering,” *IEEE Transactions on*, vol. 11, no. 1, pp. 43-53, 2003.

[17] E. Tönük, and M. B. Silver-Thorn, “Nonlinear viscoelastic material property estimation of lower extremity residual limb tissues,” *Journal of biomechanical engineering*, vol. 126, no. (2), pp. 289-300, 2004.

[18] S. Avril, L. Bouten, L. Dubuis, S. Drapier, and J. F.Pouget, “Mixed experimental and numerical approach for characterizing the biomechanical response of the human leg under elastic compression,” *Journal of biomechanical engineering*, vol. 132, no. 3, pp. 31006-31014, 2010.

[19] H. V. Tran, F. Charleux, M. Rachik, A. Ehrlacher, and M.-C. Ho Ba Tho, “In vivo characterization of the mechanical properties of human skin derived from MRI and indentation techniques,” *Computer methods in biomechanics and biomedical engineering*, vol. 10, no. 6, pp. 401-407, 2007.

[20] E. A. Zerhouni, D. M. Parish, W. J. Rogers, A. Yang, and E. P. Shapiro, “Human heart: tagging with MR imaging - A method for noninvasive assessment of myocardial motion,” *Radiology*, vol. 169, no. 1, pp. 59-63, 1988.

[21] Y. Fu, C. Chui, C. Teo, and E. Kobayashi, "Motion tracking and strain map computation for quasi-static magnetic resonance elastography," *Medical Image Computing and Computer-Assisted Intervention-MICCAI 2011*, pp. 428-435, 2011.

[22] K. M. Moerman, A. M. J. Sprengers, C. K. Simms, R. M. Lamerichs, J. Stoker, and A. J. Nederveen, "Validation of SPAMM tagged MRI based measurement of 3D soft tissue deformation," *Medical Physics*, vol. 38, pp. 1248-1260, 2011.

[23] K. M. Moerman, A. M. J. Sprengers, A. J. Nederveen, and C. K. Simms, "A novel MRI compatible soft tissue indentor and fibre Bragg grating force sensor," *Medical Engineering & Physics*, vol. 35, no. 4, pp. 486-499, 2013.

[24] I. Céspedes, J. Ophir, H. Ponnekanti and N.F. Maklad, "Elastography: elasticity imaging using ultrasound with application to muscle and breast in vivo," *Ultrasonic Imaging*, Vol. 15, no. 2, pp. 73-88, 1993

[25] J. Ophir, I. Cespedes, H. Ponnekanti, Y. Yazdi, and X. Li, "Elastography: a quantitative method for imaging the elasticity of biological tissues," *Ultrasonic imaging*, vol. 13, no. 2, pp. 111-134, 1991.

[26] H. Ponnekanti, J. Ophir, and I. Cespedes, "Axial stress distributions between coaxial compressors in elastography: an analytical model," *Ultrasound in medicine & biology*, vol. 18, no. 8, pp. 667-673, 1992.

[27] H. Ponnekanti, J. Ophir, and I. Cespedes, "Ultrasonic imaging of the stress distribution in elastic media due to an external compressor," *Ultrasound in medicine & biology*, vol. 20, no. 1, pp. 27-33, 1994.

[28] J. Jiang, and T. J. Hall, "A parallelizable real-time motion tracking algorithm with applications to ultrasonic strain imaging," *Physics in medicine and biology*, vol. 52, no. 13, pp. 3773-3790, 2007.

[29] Y. Zhu, and T. J. Hall, “A modified block matching method for real-time freehand strain imaging,” *Ultrasonic Imaging*, vol. 24, no. 3, pp. 161-176, 2002.

[30] T. J. Hall, P. Barbone, A. A. Oberai, J. Jiang, J. F. Dord, S. Goenezen, and T. G. Fisher, “Recent results in nonlinear strain and modulus imaging,” *Current medical imaging reviews*, vol. 7, no. 4, pp. 313-327, 2011.

[31] T. Z. Pavan, E. L. Madsen, G. R. Frank, A. A. O. Carneiro, and T. J. Hall, “Nonlinear elastic behavior of phantom materials for elastography,” *Physics in medicine and biology*, vol. 55, no. 9, pp. 2679-2692, 2010.

[32] T. Z. Pavan, E. L. Madsen, G. R. Frank, J. Jiang, A. A. Carneiro, and T. J. Hall, “A nonlinear elasticity phantom containing spherical inclusions,” *Physics in medicine & biology*, vol. 57, no. 15, pp. 4787-4804, 2012.

[33] P. E. Barbone, and A. A. Oberai, “Elastic modulus imaging: some exact solutions of the compressible elastography inverse problem,” *Physics in medicine and biology*, vol. 52, no. 6, pp. 1577-1593, 2007.

[34] A. A. Oberai, N. H. Gokhale, S. Goenezen, P. E. Barbone, T. J. Hall, A. M. Sommer, and J. Jiang, “Linear and nonlinear elasticity imaging of soft tissue in vivo: demonstration of feasibility,” *Physics in medicine and biology*, vol. 54, no. 5, pp. 1191-1207, 2009.

[35] F. Hild, and S. Roux, “Digital image correlation: from displacement measurement to identification of elastic properties - a review,” *Strain*, vol. 42, no. 2, pp. 69-80, 2006.

[36] F. Hild, and S. Roux, “Correli Q4: A software for-finite-element-displacement field measurements by digital image correlation,” Internal repart (269), 2008.

[37] L. Slane and D. Thelen, "The use of 2D ultrasound elastography for measuring tendon motion and strain," *Journal of Biomechanics*, vol. 47, no. 3, pp 750-754, 2014.

[38] Y. Han, D. W. Kim, and H. J. Kwon, “Application of digital image cross-correlation and smoothing function to the diagnosis of breast cancer,” J*ournal of the mechanical behavior of biomedical materials*, vol. 14, pp. 7-18, 2012.

[39] J.-S. Affagard, “Identification des propriétés hyperélastiques des muscles de la cuisse à l’état passif: couplage des techniques de corrélation d’images aux techniques d’imagerie médicale,” PhD thesis, Université de Technologie de Compiègne, Compiègne, 2013.

[40] J.-S. Affagard, S. F. Bensamoun, and P. Feissel, “Development of an inverse approach for the characterization of in vivo mechanical properties of the lower limb muscles,” to be published.

[41] W. S. Cleveland, and C. Loader, “Smoothing by local regression: Principles and methods,” Springer, 1995.

[42] S. Avril, P. Feissel, F. Pierron, P. Villon, “Estimation of the strain field from full-field displacement noisy data," *European Journal of Computational Mechanics*, vol. 17, no. 5-7, pp. 857-868, 2008.

[43] B. Nayroles, G. Touzot, and P. Villon, “La méthode des éléments diffus,” Comptes rendus de l'Académie des sciences. Série 2, Mécanique, Physique, Chimie, Sciences de l'univers, Sciences de la Terre, vol. 313, no. 2, pp. 133-138, 1991.

[44] J. D. Eshelby, “The determination of the elastic field of an ellipsoidal inclusion, and related problems,” Proceedings of the Royal Society of London, Series A, *Mathematical and Physical Sciences*, vol. 241, no. 1226, pp. 376-396, 1957.

[45] J. D. Eshelby, “The elastic field outside an ellipsoidal inclusion,” Proceedings of the Royal Society of London, Series A, *Mathematical and Physical Sciences*, pp. 561-569, 1959.

[46] P. Feissel, J. Schneider, Z. Aboura, and P. Villon, “Use of diffuse approximation on DIC for early damage detection in 3D carbon/epoxy composites,” *Composites Science and Technology*, vol. 88, pp. 16-25, 2013.

FIGURES

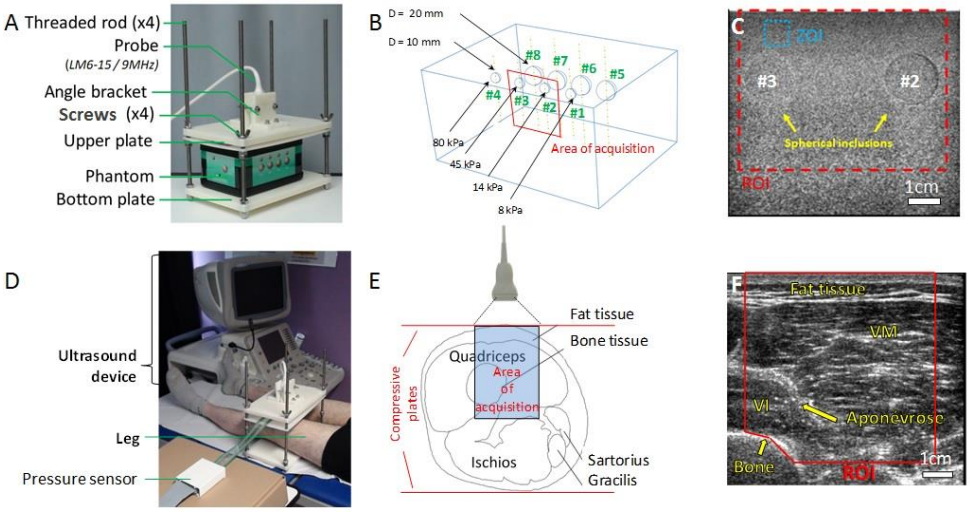

Fig. 1. (a) Home-made compression device applied to the phantom. (b) Phantom technical drawing (CIRS, Norfolk, VA). (c) Ultrasound acquisition of the phantom. (d) Home-made compression device applied to the thigh. (e) Localization of the investigated thigh muscles. (f) Thigh ultrasound acquisition of the target muscle (VM: *Vastus Medialis*, VI: *Vastus Intermedius*).

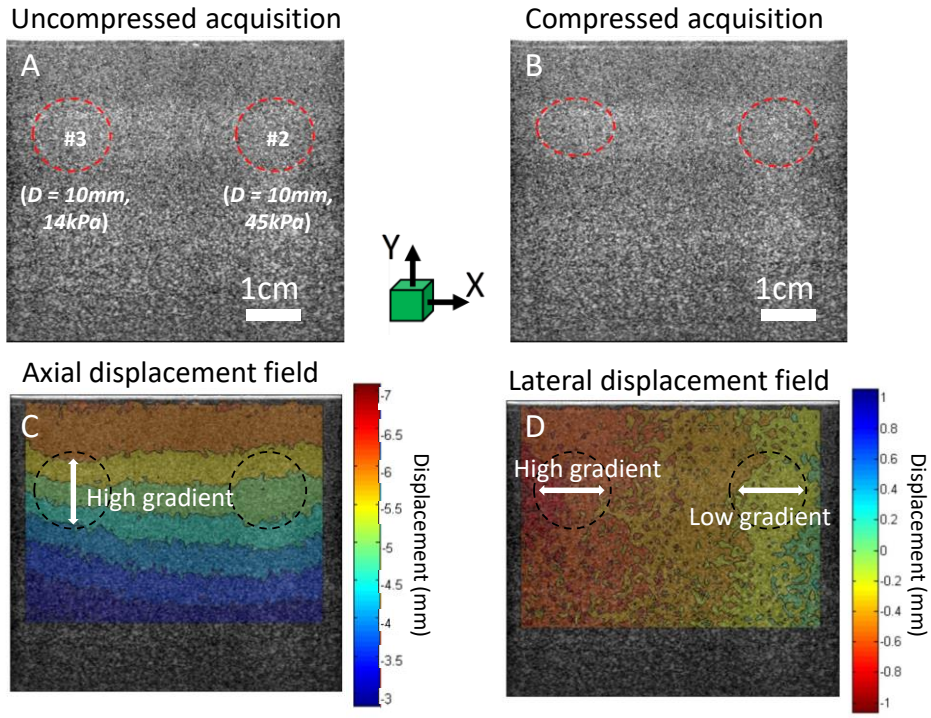

Fig. 2. Ultrasound images of (a) uncompressed and (b) compressed phantom. Cartographies of the displacement fields along the axial (c) and lateral (d) axis.

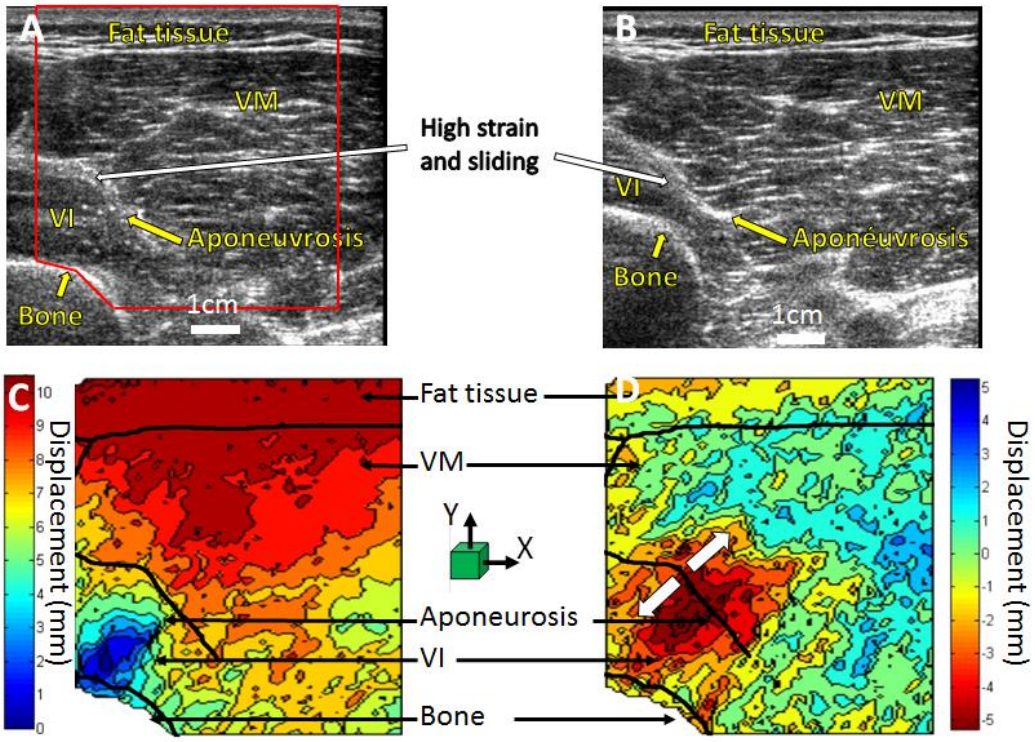

Fig. 3. Ultrasound images of uncompressed (a) and compressed (b) quadriceps muscles composed of the Vastus Intermedius (VI) and the Vastus Medialis (VM). Cartographies of the displacement fields obtained along the axial (c) and lateral (d) axis

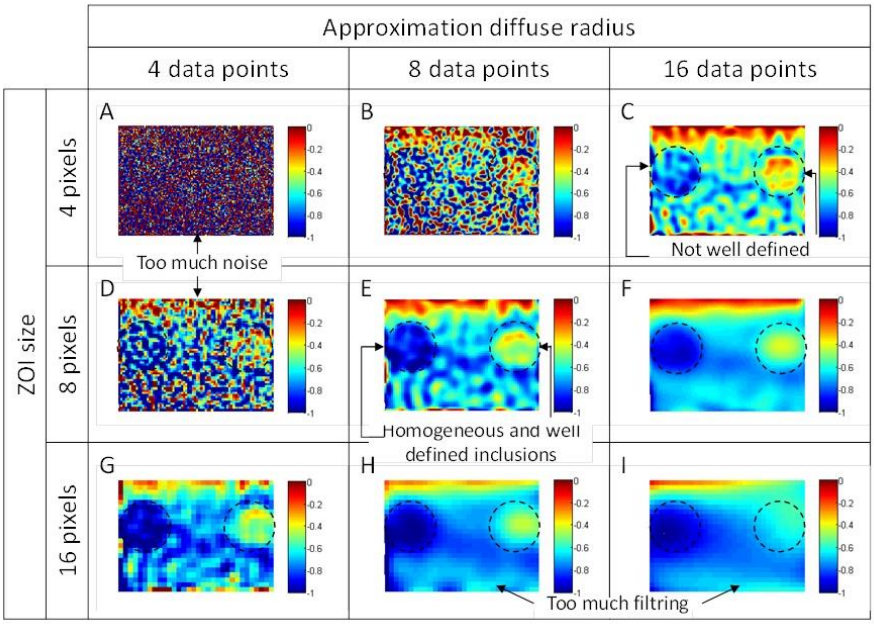

Fig. 4. Cartographies of the shear strain fields as a function of the ZOI size (4, 8 and 16 pixels) and the radius (4, 8, 16 data points).

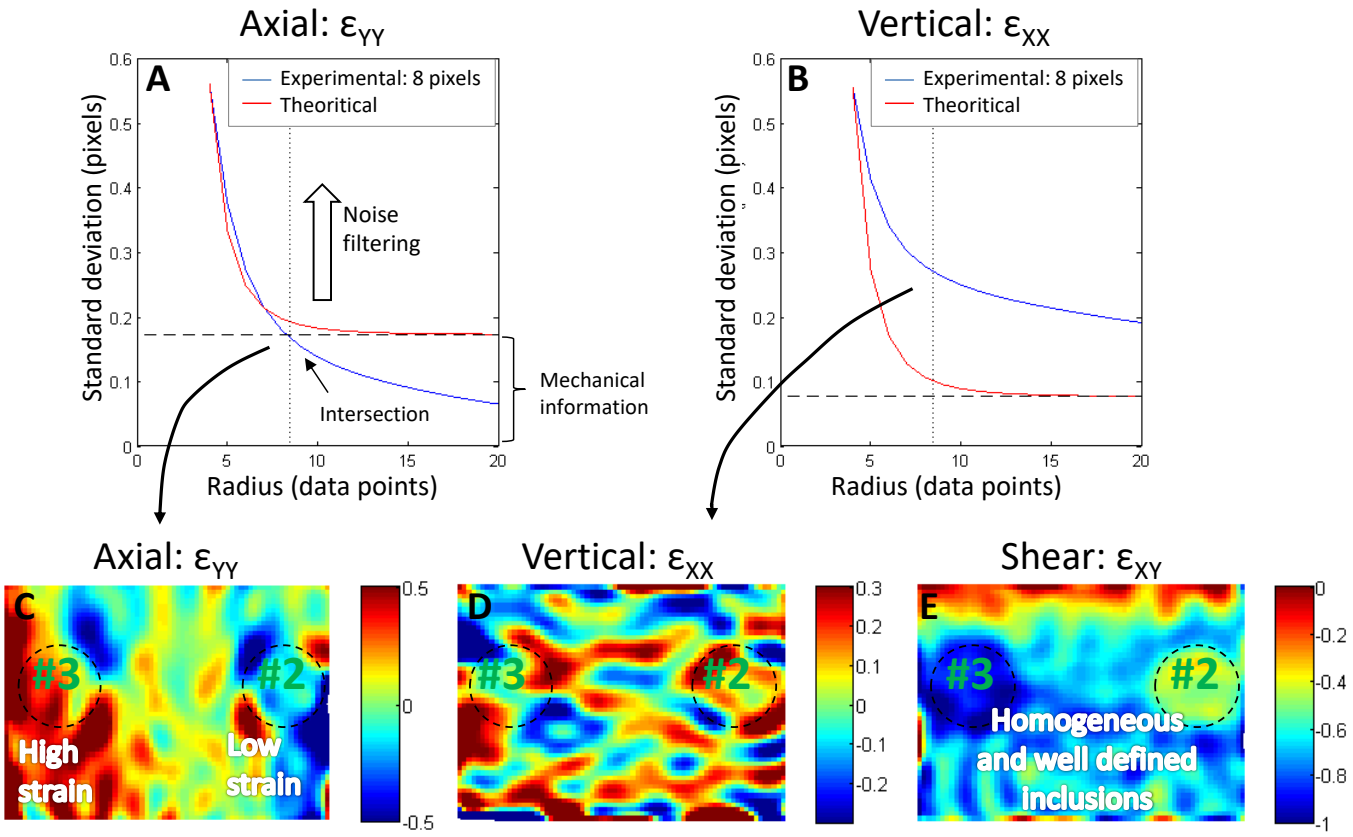

Fig. 5. Evolution of the experimental (blue) and theoretical (red) standard deviation for a ZOI of 8 pixels during an axial (a) and lateral (b) strain. Cartographies of the axial (c), lateral (d) and shear (e) strain obtained for a ZOI of 8 pixels and a radius of 9 pixels.

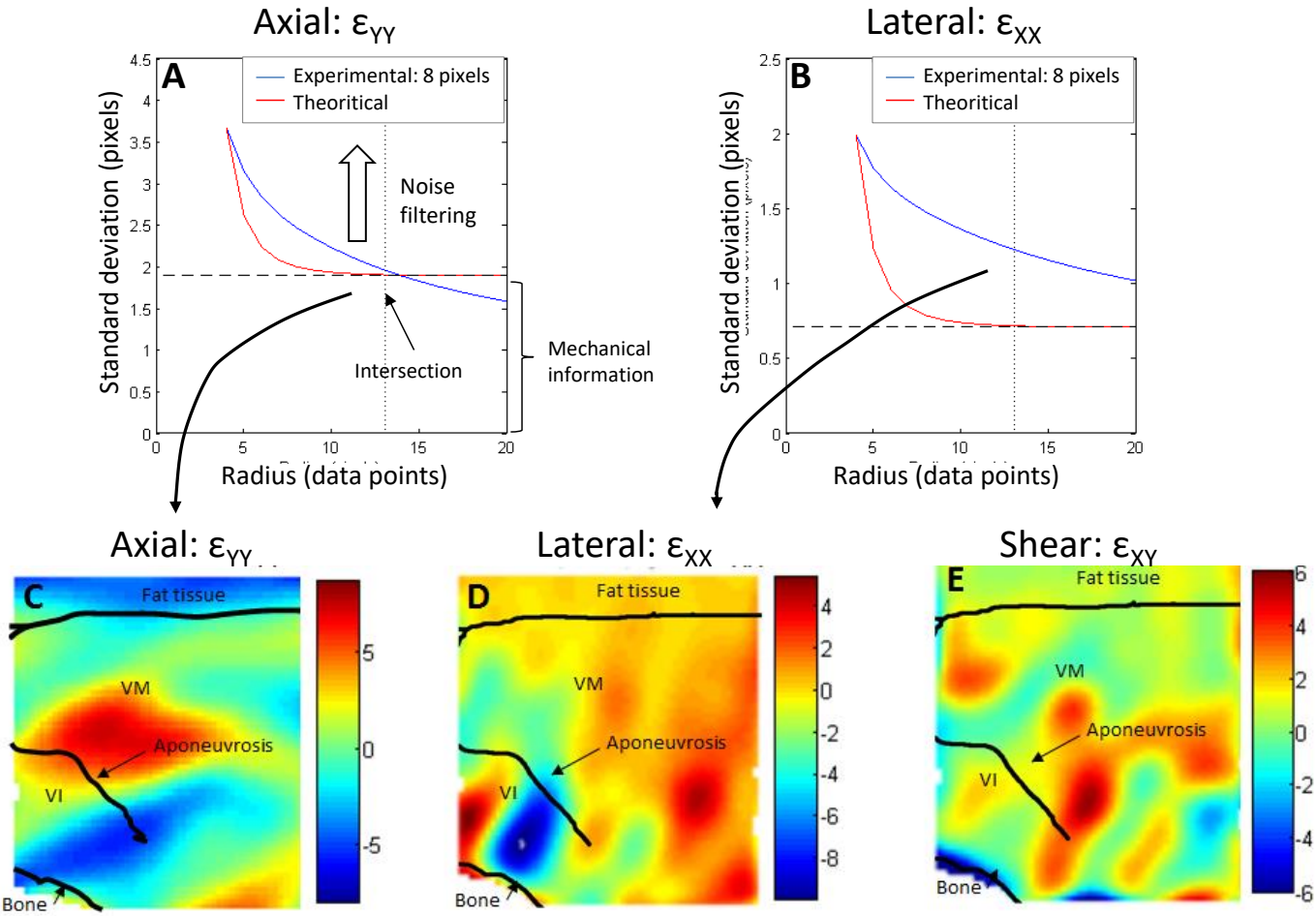

Fig. 6. Evolution of the experimental (blue) and theoretical (red) standard deviation for a ZOI of 8 pixels during an axial (a) and lateral (b) strain. Cartographies of the axial (c), lateral (d) and shear (e) strain obtained for a ZOI of 8 pixels and a radius of 13 pixels.